BRDF Models to Predict Spectral Reflectance and Emissivity in the Thermal Infrared

William C. Snyder, *Member, IEEE,* and Zhengming Wan, *Member, IEEE*

***Abstract*—This paper presents modifications to the linear kernel bidirectional reflectance distribution function (BRDF) models from Roujean *et al.* and from Wanner *et al.* that extend the spectral range into the thermal infrared (TIR). Our application is to synthesize the TIR optical properties of a scene pixel from laboratory component measurements. The angular reflectance and emissivity are needed to convert the radiance of a pixel as measured from space to land-surface temperature. The kernel models will be applied to develop a look-up table for the MODIS land-surface temperature algorithm to estimate the spectral, angular scene emissivity from land cover classification. A shrub scene and a dense canopy scene illustrate qualitative differences in angular emissivity that would not be evident without the kernel model modifications. We conclude that the modified models provide a simple and efficient way to estimate scene optical properties over a wide spectral range.**

***Index Terms*—Bidirectional reflectance, emissivity, thermal infrared.**

I. Introduction

THE bidirectional reflectance distribution function (BRDF) characterizes surface reflectance for all combinations of incident and reflected angles. The BRDF may be integrated over source and detector solid angles to get measurable optical properties, such as biconical reflectance, as defined in Nicodemus' National Bureau of Standards monograph [1]. A common application of BRDF modeling is to eliminate the effects of a particular sun-sensor geometry. This involves fitting the model to measured data and inverting it. Our application, on the other hand, is a forward synthesis to relate component properties to those of a structured surface. This paper presents modifications to a certain class of BRDF models that were developed for reflective band inversion. These modifications extend their spectral range into the 3–14-μm thermal infrared (TIR) region. The TIR versions are useful for land surface temperature because we can predict the spectral BRDF and integrate to get directional-hemispherical reflectance and emissivity of a canopy from laboratory measurements of leaves and soils and from the land-cover classification.

It is difficult over large areas to measure the reflectance and emissivity of complex land cover types. This is especially true in the thermal infrared where both the reflected and emitted radiances are significant. Many component measurements by Salisbury and others are available, however, for use in BRDF models [2]–[7]. These include high-resolution spectra of leaves, soil, sand, ice, water, snow, and rock, and so forth. There is no fundamental difference in the physics and optics used in the model derivations in going from the visible to the thermal infrared. Some of the assumptions are different because of the differences in optical properties and the differences in the application. In particular, our changes accommodate reflectance contrast reversals among components over the 3–5- and 8–14-μm atmospheric windows and focus on the use of BRDF as an intermediate step to find directional-hemispherical reflectance and emissivity.

Generally, the BRDF anisotropy is a function of component reflectance, which in turn is a function of wavelength. This shape dependence on reflectance and wavelength is primarily because of the nonlinearities inherent in multiple scattering. A linear kernel approximation, however, was developed and explored in models described by Nilson and Kuusk [8], Roujean *et al.* [9], Wanner *et al.*, and Lewis [12]. A linear combination of fixed-shape kernels is useful because it provides a simple, practical way to synthesize, integrate, and invert the BRDF. Linear kernels also provide a simple means for combining scene properties in mixed pixels by weighted linear combinations [9].

The kernel shapes arise from a structural description of the surface. The weights in the forward synthesis are developed from component reflectance and transmission, as well as structural variables. The weights also may be determined empirically from fitting the kernels to goniometer, aerial, or satellite measurements. The kernels are usually developed from more general nonlinear models by invoking linearizing approximations. With linear models, the representation of spectral BRDF is reduced to the value of several coefficients as a function of wavelength. This representation is easy to integrate by precomputing the kernel integrals, multiplying by the coefficients, and summing the terms [9]. This gives the spectral, directional-hemispherical reflectance and emissivity. A linear combination of fixed kernel shapes, however, cannot account for the nonlinearities caused by multiple scattering. But these are usually small for natural materials in the thermal

Manuscript received July 1, 1996; revised December 19, 1996. This work was performed at the Institute for Computational Earth System Science, University of California, Santa Barbara and supported by Earth Observing System Program Contract NAS5-31370 of the National Aeronautics and Space Administration.

W. C. Snyder is with GDE Systems, Incorporated, San Diego, CA 92150-9008 USA (e-mail: will@alumni.caltech.edu).

Z. Wan is with the Institute for Computational Earth Systems Science, University of California, Santa Barbara, CA 93106 USA (e-mail: wan@icess.ucsb.edu).

Publisher Item Identifier S 0196-2892(98)00139-9.

infrared because the single-scattering reflectance is typically below 10%.

These models were derived for the solar-reflective region of the electromagnetic spectrum, but are applicable over a wider spectral range with the straightforward modifications we present. The wide-range versions provide needed physical and empirical relations between libraries of component spectra, land-cover classification, and pixel reflectance and emissivity. Our goal is to predict absolute angular emissivity with a look-up table based on land-cover classification and other factors. This will be used in a split-window land surface temperature algorithm that was developed for 1-km EOS/MODIS data [13]. We also plan to use these models to determine the emissivity variations within a particular class for temperature error assessment.

Our modifications are to the Wanner kernel version of Li and Strahler's sphere-plane geometrical model and to Roujean *et al.*'s volumetric kernel model. The main difference is to keep separate some of the terms and thus eliminate assumptions about the relative magnitude of component properties. This was not done in the visible versions because it increases the number of kernels, which is problematic for inversion. The results give new kernel expressions and the corresponding coefficients. We also rederived the geometrical model to be reciprocal. A reciprocal model is one which gives the same value of the BRDF when the incident and reflected angles are switched. Our application models the BRDF, integrates the modeled BRDF to get the directional-hemispherical reflectance, and applies Kirchhoff's law to compute the emissivity from the reflectance. With nonreciprocal models, Kirchhoff's law is not guaranteed to hold. It would need to be imposed as an additional constraint on the model expressions. The applicibility of the various forms of Kirchhoff's law are proved in many texts by the use of isothermal enclosure calculations. Such techniques have been proposed for demonstrating reciprocity [14], but they are flawed—there is no general thermodynamic proof [15], [16].

Reflectance reciprocity is asserted in many optical and remote sensing texts as an extension of Helmholtz reciprocity [17]–[19]. Several other works reference DeHoop's theorem, which applies to the case of simple electromagnetic scattering [20]. Reflectance reciprocity also results from other models of electromagnetic scattering, such as Fresnel reflectance. There are no conclusive measurements of reciprocity violation under appropriate conditions, even for materials with rough surfaces that have multiple scattering [16], [21]. These laboratory measurements account for polarization and do not involve optically active materials. An important issue for Earth science is the applicibility of reciprocity to structured natural land cover types at satellite instrument resolutions.

Nicodemus provides a definition of the average BRDF that is appropriate for structured surfaces [1]. It is equivalent to the radiance-to-irradiance ratio averaged over a large area. The BRDF is taken at a horizontal reference plane above all structure. Define $d\Phi_i$ to be the incident flux per unit solid angle from an angle (θ_i, ϕ_i) on an element dA_i centered at (x_i, y_i) on a horizontal reference plane, as illustrated in Fig. 1. If the reflected radiance which comes from this incident flux is dL_r in the direction (θ_r, ϕ_r) at the point of observation, (x_r, y_r), we have the linear relation that defines the bidirectional scattering-surface reflectance-distribution function (BSSRDF) S

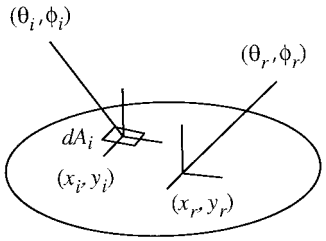

Fig. 1. The simplified geometry definitions for BSSRDF.

$$S(\theta_i, \phi_i, x_i, y_i; \theta_r, \phi_r, x_r, y_r) = dL_r / d\Phi_i. \tag{1}$$

The average BRDF for structured surfaces is then defined by the integral of the BSSRDF over an appropriate averaging area. This area depends on the scale of the material structure and is simply large enough so that the resulting average BRDF is independent of the point of observation. Here, the integral is over the incident positions for a fixed observation point

$$f(\theta_i, \phi_i; \theta_r, \phi_r) = \int_{A_i} S(\theta_i, \phi_i, x_i, y_i; \theta_r, \phi_r, x_r, y_r)\, dA_i. \tag{2}$$

It is evident from (2) that if S is reciprocal, in other words, if

$$\begin{aligned} &S(\theta_i, \phi_i, x_i, y_i; \theta_r, \phi_r, x_r, y_r) \\ &\quad = S(\theta_r, \phi_r, x_r, y_r; \theta_i, \phi_i, x_i, y_i) \end{aligned} \tag{3}$$

then the integrated average BRDF is also reciprocal

$$f(\theta_i, \phi_i; \theta_r, \phi_r) = f(\theta_r, \phi_r; \theta_i, \phi_i) \tag{4}$$

We cannot prove in general that a material will have a reciprocal BRDF, but reciprocity holds for common materials. If it does hold, then for the single scattering case of a structure of common materials, each BSSRDF path is reciprocal. Any arbitrary combination of incident angle, reference surface locations, and output angle defines a transfer geometry at some scattering element on the surface structure, or it defines a blocked path. In the case of a blocked path, the transfer is zero in both directions, so it is reciprocal trivially. In the case of a single-reflection path, reciprocity of the BSSRDF can be shown by straightforward radiometric calculations. The case for multiple scattering with opaque and translucent materials also gives reciprocal BSSRDF paths, but is more difficult to show and is addressed separately by Snyder [22]. Thus all BSSRDF paths are reciprocal, and so the average BRDF is reciprocal. Later forms of the Wanner *et al.* geometrical models invoke approximations for the inversion application that make them not reciprocal, such as the kernel versions of the Li-Sparse and Li-Dense models [10], [23]. The Li-Sparse model

presented here is rederived to keep it reciprocal. All terms of the volumetric model and the specular model are already reciprocal.

II. Kernel Models

Although the models will be reciprocal, the approximations made put into question the use of these models for the forward estimation of scene properties. The errors due to approximations are not as important for empirical fitting as they are in the forward synthesis application. In the treatment of variations in component reflectance and transmission, however, our approximations are less severe than those that were required for inversion in the original models. The problem of synthesizing scene properties is a difficult one and solutions are all but nonexistent in the infrared. If few other methods are available, an approximate method is tolerable. We defend the remaining approximations with the following observations. Our use integrates the kernels which will tend to reduce the effects of localized BRDF inaccuracies. In addition, the model estimates reduce to the expected values, such as ground BRDF, in the limiting cases, and the model predictions appear to be reasonable for the intermediate cases. Furthermore, the scene reflectance is bounded by the component reflectance, which is low to begin with for vegetation, so absolute errors in reflectance will be small. Finally, the models are useful not only for absolute estimates, but also for studying qualitative effects, finding regression trends, and determining relative variations. Relative differences are likely to be modeled more accurately.

We modified expressions for a sphere-plane geometrical model, a volumetric model, and a rough-specular model. The associated structures are shown in Fig. 2. The symbols in this figure correspond to those defined later in the derivations. The geometrical model is applied to classes with sparse shrubs, trees, or crops with a soil or soil-grass understory. The sphere and understory reflectances are calculated from the volumetric model applied to the leaf and soil components. For the sphere, the volumetric optical depth is taken to be infinite. For the understory, the volumetric model estimates are based on vegetation coverage. The resulting nadir directional-hemispherical reflectances from the volumetric model are taken to be Lambertian and applied to the geometric model. The sphere-plane approach also works well, at least empirically, for bare soils [24]. The volumetric model treats a homogeneous layer of isotropically oriented facets (leaves) with some density related to leaf area index (LAI) and some reflectance and transmission. The lower boundary is a Lambertian reflectance which could be a direct measurement of bare soil, or a separate volumetric model estimate of grass, or soil litter. The specular model is a Fresnel surface with a specified roughness that disperses the specular reflection. This is suitable for forward modeling of water or ice.

In the kernel approach, the BRDF is a weighted linear combination of fixed kernel shapes and a constant kernel (isotropic). The weight values depend on component fractional areas, structural properties, and reflectances. By convention all kernels except the isotropic are normalized to be zero at zero incident and reflected zenith angles [9]. The isotropic kernel is

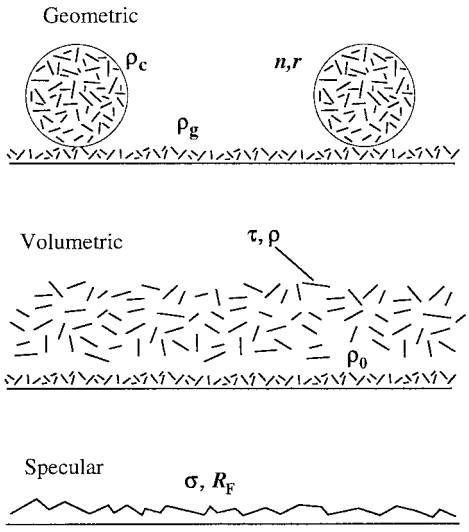

Fig. 2. The scene structures for the geometrical, volumetric, and specular BRDF models. For the geometric case, ρ_c is the Lambertian crown reflectance from the volumetric model, and ρ_g is the Lambertian ground reflectance from the volumetric model or direct measurements. The variables n and r are the number density and radius of the crowns, respectively. For the volumetric model, the randomly oriented facets have a reflectance ρ and a transmission τ. The understory reflectance ρ_0 is from either a volumetric estimate or from direct measurements. The specular model applies the Fresnel reflectance of the surface R_f and a roughness parameter σ.

normalized to unity. In these derivations, we will assume that only the relative azimuth between the incident and reflected angles ϕ need be considered. The zenith angles of incidence and reflection are θ_i and θ_r, respectively. The scattering angle between incidence and reflection is given by

$$\xi = \arccos(\cos\theta_i \cos\theta_r + \sin\theta_i \sin\theta_r \cos\phi). \tag{5}$$

For the following expressions, f is the BRDF, k is the fixed-shape kernel, and c is the weight value. All radiometric quantities are spectral.

A. Isotropic Kernel

The isotropic BRDF is

$$f_{\text{iso}} = c_1 k_{\text{iso}} \tag{6}$$

where the kernel is simply

$$k_{\text{iso}} = 1.0. \tag{7}$$

B. Geometrical Model

Our geometric kernel is based on the Li and Strahler sparse canopy model [23]. The derivation closely follows Wanner's kernel version of the Li-Sparse model [10]. We omit the Li-Dense case because, for reflectance and emissivity in the thermal infrared, the volumetric effects of the crowns and understory dominate the optical properties. For the dense crown case, we simply apply the volumetric model. When the models are integrated, the differences in doing this are small. The original models were derived in terms of reflectance.

Our derivation takes a different approach because it begins by applying the simple BRDF relation: $f = L/(E_0 \cos\theta_i)$. The goal is to find an expression for the radiance L given the illumination irradiance E_0 and the illumination zenith angle θ_i.

The more general geometrical model considers a plane with spheroids (canopy crowns) of variable number density, variable aspect ratio, and variable height above a plane. The shaded areas are taken to be black, and the reflectance of the spheroids and plane are taken to be equal. We will consider only the case of spheres on a plane for which there are n per unit area with radius r. We neglect the mutual shadowing effects, as is appropriate in the sparse model, and compute the projected viewed and illuminated areas directly, not by Boolean probabilities, as introduced by Strahler and Jupp [25]. We will keep the model separated into two kernels, however, by not combining the contributions from the illuminated ground and the illuminated sphere. Although the reflectances of the two are often the same, they are not for shrubs in arid areas where the understory is sand. In the TIR, sand has a much higher reflectance than vegetation in certain regions of the spectrum. The separated version will result in two new shaped kernels and three new coefficients (the third for the isotropic portion).

The average spectral radiance viewed from some angle is the projected area-weighted sum of the radiances of the two illuminated components

$$L = F_g L_g + F_c L_c \tag{8}$$

where F_g and F_c are the viewed fractions of illuminated ground and crown area, respectively. If this radiance was produced by a collimated irradiance E_0 in the plane normal to incidence, the BRDF for given incident and reflected angles is given by

$$\begin{aligned} f_{\text{geo}} &= \frac{L}{E_0 \cos\theta_i} \\ &= F_g \frac{L_g}{E_0 \cos\theta_i} + F_c \frac{L_c}{E_0 \cos\theta_i}. \end{aligned} \tag{9}$$

For the ground, $L_g = f_g E_0 \cos\theta_i$. If f_g is isotropic, $L_g = (\rho_g/\pi) E_0 \cos\theta_i$, where ρ_g is the Lambertian reflectance of the ground. The radiance for the crown spheres is not as easy. We must account for the lower radiance near the edges of the sphere by averaging the radiance over the projected disk. Also, we must account for the fact that the irradiance intercepted by the sphere does not diminish with increasing source zenith angle as it does for the plane. If the sphere surface has a Lambertian reflectance ρ_c it can be shown by integration that the average radiance of the sphere as viewed from the source direction is

$$L_c = \frac{2}{3} \frac{\rho_c}{\pi} E_0. \tag{10}$$

Substituting this into (9) gives

$$f_{\text{geo}} = F_g \frac{\rho_g}{\pi} + F_c \frac{\rho_c}{\pi} \frac{2}{3} \sec\theta_i. \tag{11}$$

Next, we will derive the fraction of the total viewed area occupied by illuminated ground F_g. We find this by examining the projections of spheres onto the plane. The expression is

$$F_g = 1 - n(A_r + A_i - A_r \cap A_i) \tag{12}$$

where A_r is the projected area of the sphere onto the plane from the reflected direction and A_i is the projected area of the sphere onto the plane from the incident direction. We must subtract the intersection of these areas. The area of an ellipse is πab where a and b are the major and minor axes. The major axis of the projection is $r \sec\theta$. The minor axis is r, so the projected areas are $A_i = \pi r^2 \sec\theta_i$ and $A_r = \pi r^2 \sec\theta_r$. The intersection is a difficult expression to derive. Irons *et al.* give an empirical representation [24], but Wanner develops a geometrical approximation based on parameterizing the ellipses which we employ [10]

$$A_r \cap A_i = r^2(\sec\theta_i + \sec\theta_r)(t - \cos t \sin t) \tag{13}$$

where

$$\cos t = \frac{\sqrt{D^2 + (\tan\theta_i \tan\theta_r \sin\phi)^2}}{\sec\theta_i + \sec\theta_r} \tag{14}$$

and

$$D^2 = \tan^2\theta_i + \tan^2\theta_r - 2\tan\theta_i \tan\theta_r \cos\phi. \tag{15}$$

Thus we have defined all the terms in F_g.

Now for the fraction of the total area that is both illuminated and viewed sphere F_c. The fraction of the total area occupied by spheres is the projected area given by $n\pi r^2 \sec\theta_r$. The illuminated fraction is also from an approximation by Wanner [10]

$$F_c = n\pi r^2 \sec\theta_r \cos^2(\xi/2). \tag{16}$$

Recall that the phase angle ξ was defined in (5). This expression does not account for the distribution of irradiance over the illuminated portion of the sphere, but it is correct for $\xi = 0$ and $\xi = \pi$ and so will be taken as a sufficiently good approximation.

Substituting F_c and F_g into (11) and normalizing the kernels to zero at nadir, we have for the kernel BRDF

$$f_{\text{geo}} = c_1 k^g_{\text{geo}} + c_2 k^c_{\text{geo}} + c_3 \tag{17}$$

where the kernels are

$$\begin{aligned} k^g_{\text{geo}} = \frac{1}{\pi}(\sec\theta_i + \sec\theta_r)(t - \cos t \sin t) \\ - \sec\theta_r - \sec\theta_i + 1 \end{aligned} \tag{18}$$

and

$$k^c_{\text{geo}} = \sec\theta_r \sec\theta_i \cos^2(\xi/2) - 1 \tag{19}$$

and the coefficients are

$$c_1 = nr^2\rho_g \tag{20}$$

$$c_2 = \tfrac{2}{3} nr^2 \rho_c \tag{21}$$

and

$$c_3 = (1/\pi - nr^2)\rho_g + \tfrac{2}{3}nr^2\rho_c. \tag{22}$$

With this model we can independently adjust the ground and crown reflectance. Clearly, both kernels are reciprocal, so the model is reciprocal. We also have introduced a factor of 2/3 in the sphere radiance that does not appear in the original version.

The model may be extended to the case where the spheres become spheroids by scaling the vertical dimension to convert the spheroids back to spheres as is done in the Wanner *et al*.derivations. This transforms the zenith angles by the formula $\theta' = \tan^{-1}(b/r\ \tan\theta)$, where b and r are shape parameters [23]. The model could also be improved to account for mutual shadowing and to apply a boolean model to the fractional area formulas [23], [25].

C. Volumetric Model

Roujean *et al*. and Ross provide a volume scattering BRDF model for an isotropic distribution of facet slopes with reflectance ρ and transmission τ above a ground reflectance of ρ_0 [9], [26]. For this model, the facet number density and canopy height are represented by a structural constant F, which is related to LAI. By keeping the reflectance and transmission terms separate, the volumetric BRDF expression becomes

$$f_{\text{vol}} = \frac{2}{3\pi^2}\,\frac{[(\pi-\xi)\cos\xi+\sin\xi]\rho + (\sin\xi - \xi\cos\xi)\tau}{\cos\theta_i+\cos\theta_r} \times [1-\exp(-bF)] + \frac{\rho_0}{\pi}[\exp(-bF)]. \tag{23}$$

Here, $b = (1/2)/(\cos\theta_i + \cos\theta_r)$, but to represent the model with fixed kernels, the value of b is approximated as a constant (1.5), based on typical values of the angles. This is acceptable for medium to dense canopies where not much of the ground is viewed directly in any case.

For the visible and near infrared version, the facet (leaf) transmission is assumed equal to the reflectance ($\tau = \rho$). This reduces (23) to one kernel shape. In the thermal infrared, because of the absorption of water in green leaves, $\tau \ll \rho$ [27]. Therefore, the volumetric BRDF exhibits a broad volumetric backscattering peak. In other parts of the spectrum the transmission is larger, and the BRDF is less dependent on the incident angle with higher values at the larger view zeniths. So, we will keep the expression separated into two kernel shapes to allow τ and ρ to vary. Generally, τ will be taken to be zero from 3 to 14 μm, but the τ kernel will be included for completeness. We have

$$f_{\text{vol}} = \frac{2\rho}{3\pi^2}\,\frac{1-\exp(-bF)}{\cos\theta_i+\cos\theta_r}[(\pi-\xi)\cos\xi+\sin\xi] + \frac{2\tau}{3\pi^2}\,\frac{1-\exp(-bF)}{\cos\theta_i+\cos\theta_r}[-\xi\cos\xi+\sin\xi] + \frac{\rho_0}{\pi}\exp(-bF). \tag{24}$$

So the normalized volumetric BRDF model is

$$f_{\text{vol}} = c_1 k_{\text{vol}}^{\rho} + c_2 k_{\text{vol}}^{\tau} + c_3 \tag{25}$$

where the kernels are

$$k_{\text{vol}}^{\rho} = \frac{(\pi-\xi)\cos\xi+\sin\xi}{\cos\theta_i+\cos\theta_r} - \frac{\pi}{2} \tag{26}$$

and

$$k_{\text{vol}}^{\tau} = \frac{-\xi\cos\xi+\sin\xi}{\cos\theta_i+\cos\theta_r} \tag{27}$$

and the coefficients are

$$c_1 = \frac{2\rho}{3\pi^2}[1-\exp(-bF)] \tag{28}$$

$$c_2 = \frac{2\tau}{3\pi^2}[1-\exp(-bF)] \tag{29}$$

and

$$c_3 = \frac{\rho}{3\pi}[1-\exp(-bF)] + \frac{\rho_0}{\pi}[\exp(-bF)]. \tag{30}$$

Both kernels are reciprocal. For a given structure, their relative weights are proportional to the relative values of the reflectance and transmission of the leaves. The viewed "optical depth" $-bF$ determines the proportion of leaf and ground reflectance in the isotropic constant.

D. Specular Model

For land surfaces specular behavior occurs in several special cases. For each case, the width of the specular lobe is different so the specular component may not be accurately represented by a single, fixed kernel. The lobe width is a function of the surface slope distribution σ. Land surfaces that have a specular component include inland water bodies, water under vegetation, ice, snow, and silt (dry lake bed). The general specular kernel here is based on widely used derivations for ocean reflectance [28]. There are studies of this approach by Strahler and by Ahmad and Deering [11], [29]. The proposed Strahler version is linearized, but is not reciprocal. We begin the derivation by adapting Ahmad and Deering's reflectance to BRDF and linearizing the model with Strahler's approach. The result is a family of BRDF kernels that is parameterized by the surface roughness. The BRDF is

$$f_{\text{spc}} = \frac{R_F(\xi)P(\theta_n,\sigma)}{4\cos(\theta_i)\cos(\theta_r)\cos^4(\theta_n)}. \tag{31}$$

The probability function for seeing specular contribution in the view direction is

$$P(\theta_n,\sigma) = \frac{1}{\pi\sigma^2}\exp\left(-\frac{\tan(\theta_n)}{\sigma^2}\right) \tag{32}$$

and the specular surface normal angle is

$$\theta_n = \arccos\left(\frac{\cos(\theta_r)+\cos(\theta_i)}{2\cos(\xi/2)}\right). \tag{33}$$

With the assumption that the incident light is not polarized and that the detector is not sensitive to the polarization of the

reflected light, the Fresnel reflection is given by

$$R_F(\xi) = \frac{1}{2}\left[\frac{\sin^2(\xi/2-\alpha)}{\sin^2(\xi/2+\alpha)} + \frac{\tan^2(\xi/2-\alpha)}{\tan^2(\xi/2+\alpha)}\right]. \quad (34)$$

It turns out that the kernel shape is not changed very much with different indices of refraction so we can take $n = 1.33$ (the value for water), so in the Fresnel expression

$$\alpha = \arcsin(\tfrac{1}{1.33}\sin(\xi/2)). \quad (35)$$

Finally, the value of the specular BRDF at zero incident and reflected angles is

$$f^0_{\rm spc} = \frac{R^0_F}{4\pi\sigma^2}. \quad (36)$$

For a zero kernel value at nadir geometry, we can rewrite the expression for the BRDF that corresponds to a surface slope distribution σ as

$$f_{{\rm spc},\sigma} = c_1 k_{{\rm spc},\sigma} + c_2 \quad (37)$$

where the parameterized kernel is

$$k_{{\rm spc},\sigma} = \frac{\pi\sigma^2 R_F(\xi) P(\theta_n,\sigma)}{R^0_F \cos(\theta_i)\cos(\theta_r)\cos^4(\theta_n)} - 1 \quad (38)$$

and

$$c_1 = c_2 = \frac{R^0_F}{4\pi\sigma^2}. \quad (39)$$

Water roughness can be related to wind speed. At 5 m/s, the wind produces a surface roughness equivalent to $\sigma = 0.17$, which Strahler suggests as an approximate value for all inland water [11]. It is unknown over what range the roughness for ice varies, but it will be seen for moderate angles that the directional-hemispherical emissivity is not strongly affected by roughness for either water or ice.

III. Results

A. Qualitative Kernel Comparison

Fig. 3 is a Cartesian plot of the five shaped kernels with nadir illumination. For the geometrical kernel, the ground normally will be more reflective and the backscattering component will dominate the shape. The crown kernel shape will be more prominent in cases where the ground is less reflective than the crowns, such as for senescent foliage over certain soil types in the infrared [5]. It is clear that for moderate to large angles, the geometric BRDF strongly depends on the balance in reflectance between the ground and the crown. The two volumetric kernels are more isotropic, but again, it is clear that the BRDF values at moderate to large angles depend on the balance between the leaf reflectance and transmission. The specular BRDF kernel is plotted with $\sigma = 0.2$.

Fig. 4 shows surface plots of the five kernels and the isotropic kernel in spherical-polar coordinates. The plots represent BRDF over a range of zeniths and azimuths for a fixed directional illumination at a zenith of 30°. This incident direction is shown as a line in the first quadrant in the xz plane (upper right). The material surface is in the xy plane (bottom). The radius of the surface in any direction is proportional to the reflected radiance. The reflected zenith angles beyond approximately 75° are not plotted because some model expressions become large at these extremes. Fig. 4(a) is the isotropic kernel, which is a section of sphere in these coordinates. Fig. 4(b) is a surface plot of the specular kernel with roughness parameter $\sigma = 0.2$ and $c_1 = c_2$. The axis of the specular lobe is very nearly along the specular scattering angle and its width is a function of σ. This lobe becomes distorted at larger incident angles because of the limiting geometry of the surface. Fig. 4(c) and (d) are surface plots of the geometric ground and crown BRDF kernels, added to a nominal value of the isotropic BRDF to make all values positive. The weights are $c_1 = c_2 = 0.3c_3$. The ground kernel clearly shows the sharp backscattering peak where the source shadows disappear. The crown kernel shows broad backscattering because the illuminated portion of the sphere is centered toward the source. Fig. 4(e) and (f) show the volumetric surface plots of the ρ and τ kernels. Here again, we choose to set $c_1 = c_2 = 0.3c_3$ to illustrate the shapes. For leaves with dominant reflectance, there is a mild volumetric backscattering lobe. With a high leaf transmission, the lobe is in the specular direction.

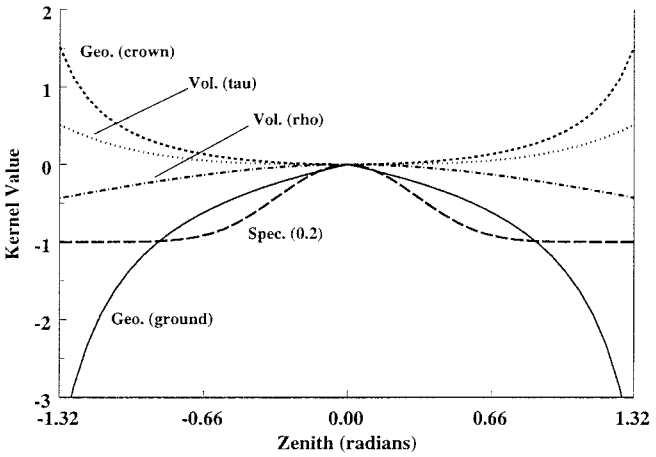

Fig. 3. The five shaped kernels plotted with nadir illumination in Cartesian coordinates. The kernels are rotationally symmetric with nadir illumination. Note that the kernel values are normalized to be zero at zero zenith.

B. Integration for Reflectance and Emissivity

For linear kernel models, the integral of the BRDF over the hemisphere for a given angle of incidence is a linear combination of the integrated kernels at the same angle and with the same weights [9]. This means that for the directional reflectance and directional emissivity, we need only integrate the kernels once for a range of incident angles and make a look-up table. Then, the reflectance is determined for a surface of interest by adding these values weighted by the spectral coefficients. The kernel integrals are plotted in Fig. 5. For all but the geometrical ground kernel, the reflectance increases with angle. For the geometrical kernel, as was the case for the BRDF shape, the directional reflectance depends strongly on the balance between the crown and ground component reflectances. For the volumetric kernel,

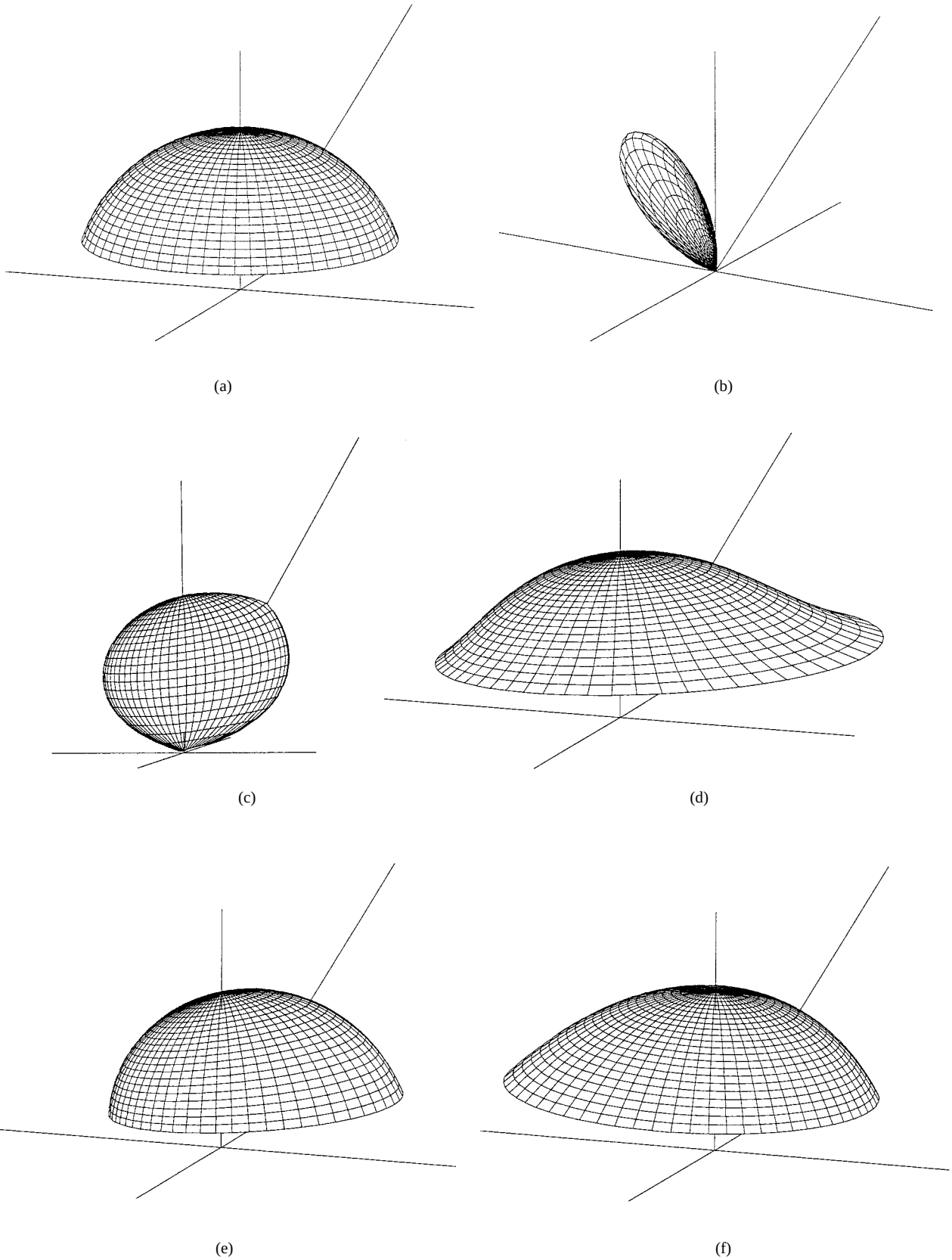

Fig. 4. Spherical-polar surface plots of the BRDF kernels with an illumination zenith angle of 30° (shown as a line from the upper right). The distance of the surface from the origin is proportional to radiance for a given incident irradiance at that geometry. The isotropic curve (a) is simply a portion of a sphere. The specular curve (b) has its major axis near the specular angle and its width is a function of the roughness. The geometric ground kernel (c) has a "backscattering peak" toward the incident direction. At this angle, all of the illuminated portion of the ground is viewed so that there is a BRDF maximum. For the geometric crown kernel (d), the BRDF also has a backscattering emphasis because the more of the illuminated portion of the crown is viewed. The volumetric reflection and transmission kernels (e) and (f) show a back and forward scattering characteristic, respectively. The backscattering from the reflection kernel is for the same reasons as before: all of the viewed facets are illuminated, and there are no shadows.

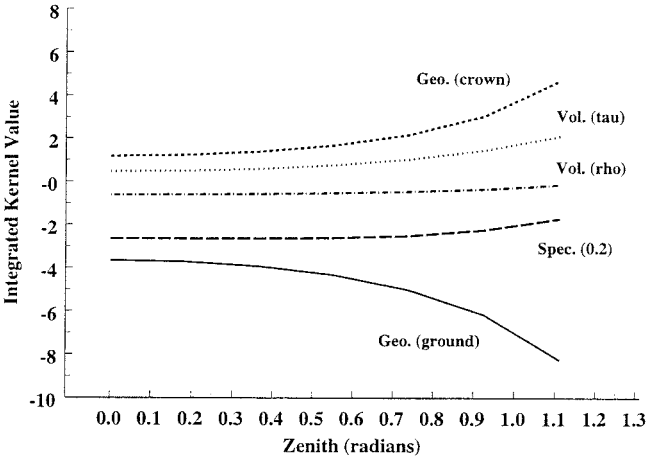

Fig. 5. The kernel integrals as a function of zenith angle in Cartesian coordinates. The integral of the isotropic kernel (not shown) is simply π. These plots correspond to the individual contributions to directional-hemispherical reflectance.

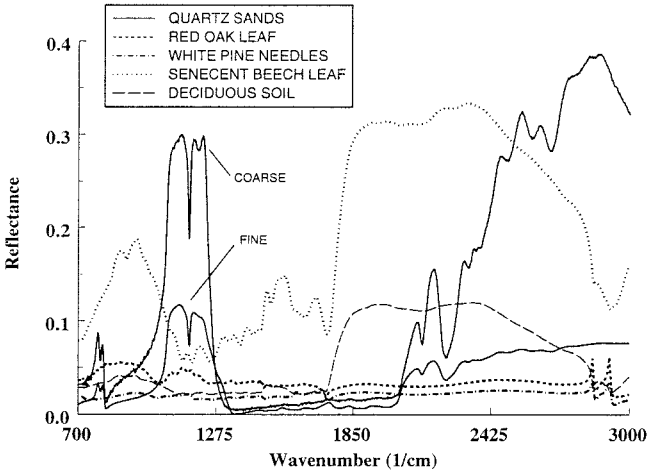

Fig. 6. Spectral reflectance of five component materials in the TIR measured with a spectrometer and an integrating sphere. The abscissa units are wavenumber—the range is approximately 14.3–3.3 μm.

the dependence of reflectance on the balance between leaf reflectance and transmission is not as strong.

C. Component Reflectance Spectra

The thermal infrared reflectance spectra of component materials may be measured with a Fourier transform infrared spectrometer and an integrating sphere system [4]. For a typical system, a silicon-carbide element is heated to approximately 1100 K to provide source illumination, which is then passed through an interferometer and directed to the material surface at the sample port of an integrating sphere. A TIR detector measures the modulation of the light amplitude as the interferometer mirror scans, resulting in an interferogram that is Fourier transformed into a power spectrum. The process is repeated with reference materials to calibrate the response of the system. The spectral resolution of the system is typically 2–8 cm^{-1} depending on the mirror distance traveled. The instrument provides the directional-hemispherical reflectance at a zenith of 10°, not at nadir, to prevent a specular return from being lost through the entrance port. The diameter of the illumination spot for a typical system is $\simeq 1$ cm, which is sufficient to measure many common component materials such as sand, gravel, soil, snow, ice, pine needles, leaf surfaces, etc. The reflectance is converted to emissivity by applying the angular form of the relation $\varepsilon = 1 - \rho$.

Fig. 6 shows the TIR reflectance spectra of five diverse materials at a 4 cm^{-1} resolution. These are from Salisbury's measurements [5], but we are also building a library of similar measurements. In wavenumber, the atmospheric windows in the TIR are approximately 2000–3000 cm^{-1} for the 3–5 μm region and 750–1250 cm^{-1} for the 8–14 μm region. Green vegetation and organic soil have the lowest reflectance. Dry vegetation and pure minerals generally have a larger spectral contrast. For instance, at the principal Christiansen feature (1350 cm^{-1}), the quartz sand has a reflectance of only 0.002, but in its restrahlen bands between 1000 and 1250 cm^{-1}, the reflectance can range from 0.05–0.40 depending on the grain size. Reflectances in the thermal infrared are typically less than 0.01 for snow to 0.01–0.06 for ice (these are not plotted) [6]. Clearly the geometrical model assumption that $\rho_g = \rho_c$ would not be valid in the TIR, for instance, with senescent foliage and deciduous soil. For sand and soils the TIR BRDF of the components has a mild backscattering lobe, but is generally isotropic [7]. Leaf surfaces are perhaps not as isotropic, but the effects of a specular component are diminished in a volume scattering medium.

D. Examples

First we will compare two cases with the geometrical BRDF scene model. One is a synthesis of sparse green (nonsenescent) pine shrubs and pure sand. The other is a synthesis of senescent shrubs and snow. This is an extreme comparison, but illustrates some interesting qualitative effects caused by the contrast reversal. We choose $nr^2 = 0.1$ and apply the component spectra to compute the spectral coefficients of the model. The reflectance of the pine shrubs is taken to be half that of the needle sample, and the senescent shrub reflectance is taken to be one-third that of the senescent leaf surface to account for the volumetric effects. Fig. 7 shows the sand/pine spectral kernel coefficients, the scene reflectances with zenith angles of 10°, 30°, and 50°, and a surface plot of the scene BRDF at 2500 cm^{-1} $(4\ \mu\text{m})$ with a zenith angle of 30°. Fig. 8 shows the same plots for the snow/senescent leaf scene.

For the sand/pine case there is a significant decrease in the quartz restrahlen signature at 50°. The reflectance decreases with increasing angle because it makes a transition from the ground signature to the crown signature as the viewed proportions change. The BRDF shows the geometrical backscattering peak of the ground kernel because the shrubs are relatively nonreflective. The reflectance of fine snow is 0.01 or less over this wavelength range, therefore, in the snow/senescent case we have inverted the relationship between ground and crown reflectance. The angular reflectance increases with increasing angle and the BRDF is dominated by the crown kernel. It is clear that if the component signatures are different there will be a significant angular variation of the reflectance. That

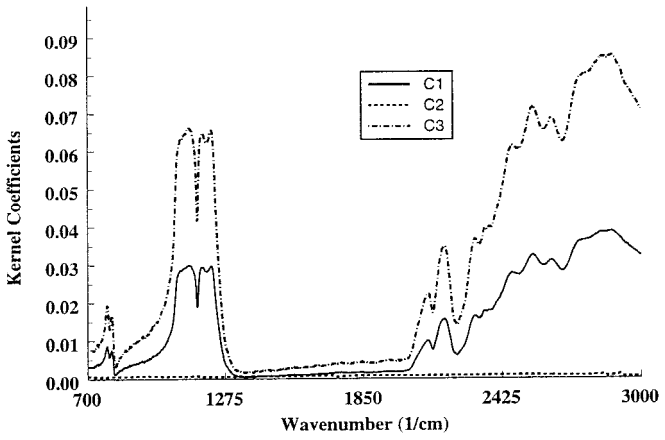

(a)

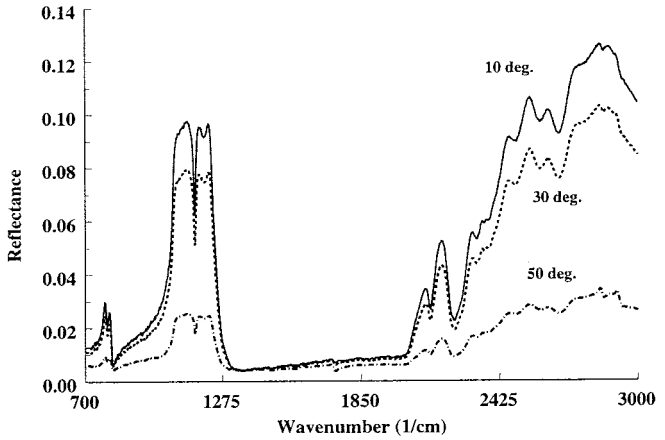

(b)

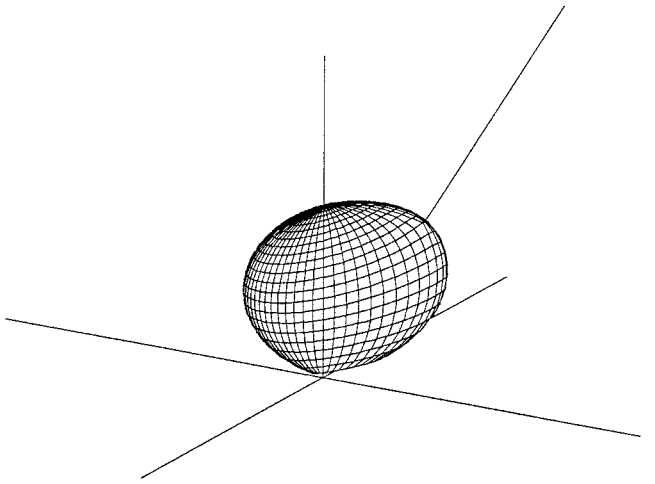

(c)

Fig. 7. Geometric sand/pine scene synthesis showing (a) the spectral kernel coefficients, (b) the angular spectral reflectances, and (c) the BRDF at 2500 cm^{-1} and 30° zenith angle.

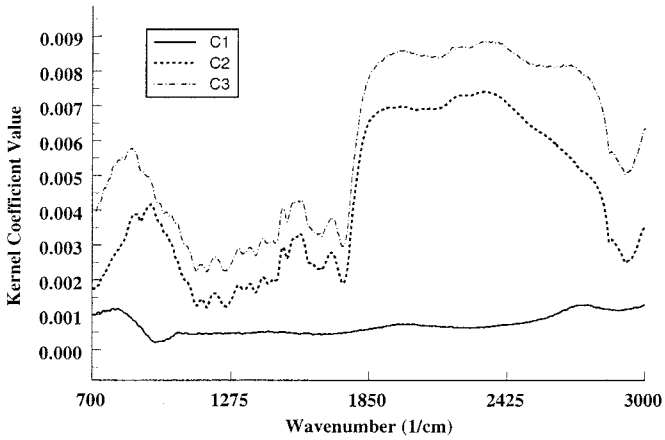

(a)

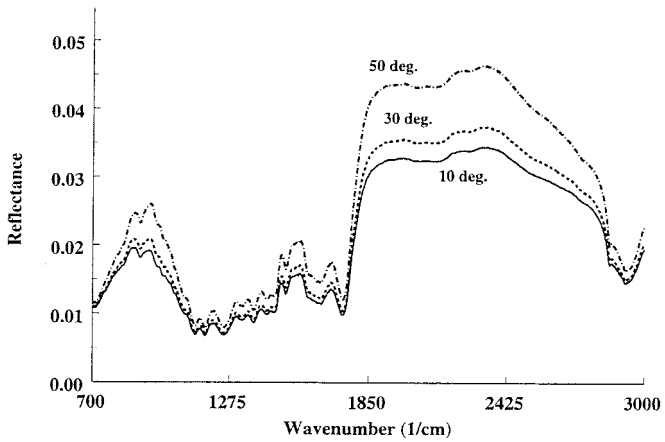

(b)

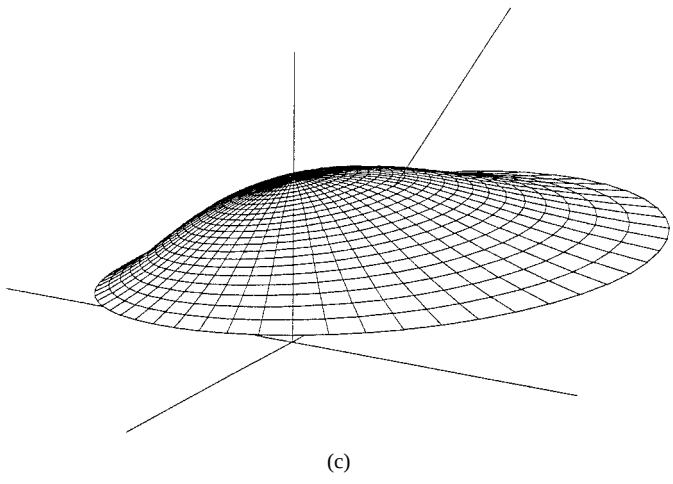

(c)

Fig. 8. Geometric snow/senescent scene synthesis showing (a) the spectral kernel coefficients, (b) the angular spectral reflectances, and (c) the BRDF at 2500 cm^{-1} and 30° zenith angle.

this can be a positive or negative dependence would not be apparent without the two-kernel geometrical model.

The volumetric case is illustrated by green oak leaves and deciduous soil. We take $\tau = 0$ over the TIR spectrum so that $c_2 = 0$. Fig. 9 illustrates the results of the volumetric synthesis with $F = \text{LAI} = 1.0$. At this LAI there will be some of the soil component present in the scene spectrum. The reflectance does not change much with angle. For high values of LAI the limiting value of nadir reflectance is $\rho/3$, so the volumetric scattering significantly reduces the reflectance. In unpublished measurements from our integrating sphere, we have found that indeed the reflectance of a leaf surface is reduced by a factor of approximately 1/3, with small, randomly stacked

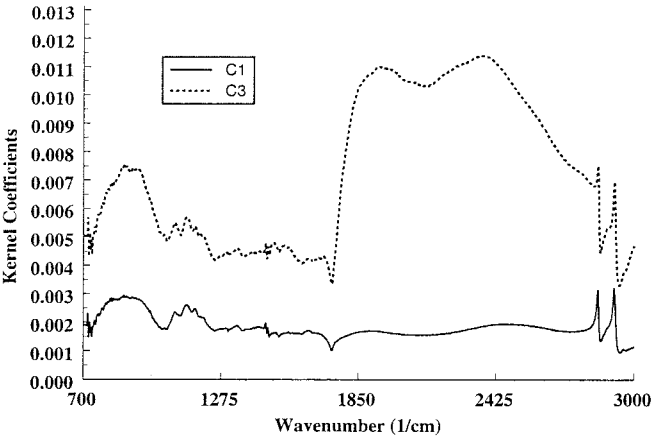

(a)

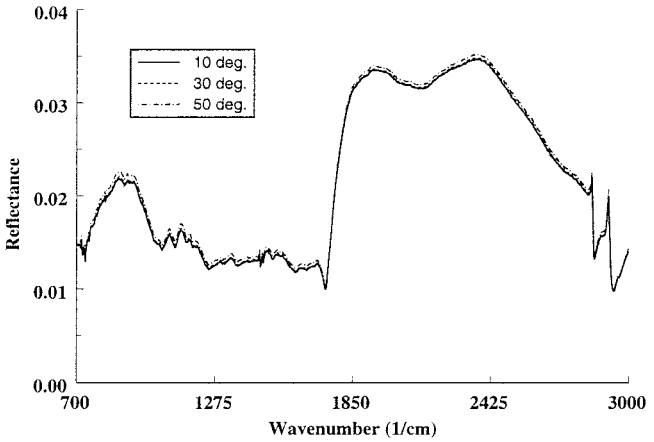

(b)

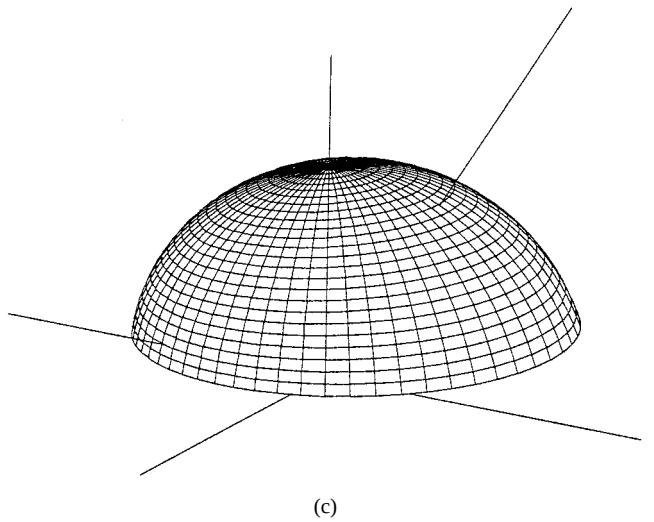

(c)

Fig. 9. Volumetric soil/oak scene synthesis showing (a) the spectral kernel coefficients, (b) the angular spectral reflectances, and (c) the BRDF at 2500 cm^{-1} and 30° zenith angle.

pieces. Green leaf component reflectance is already low and in the 8–14-μm region and the volumetric emissivity approaches unity (0.98–0.99).

E. Comparison with Measurements

The nonkernel form of the geometric model has been validated by comparison to Monte Carlo results [23]. Wanner *et al.* and Hu *et al.* provide treatments of the validity of the kernel version in the visible and near infrared [30], [31]. We have not yet validated the model for our application in the TIR. In our TIR measurements of bare soils, however, for which the model is applicable, we have found the model-predicted backscattering peak in the BRDF [7].

The volumetric predictions are consistent with medium-scale measurements using the box method over a savanna by Van de Griend *et al.* [32]. In this study, it is found that as the vegetation coverage over bare soil increases from 10% sorghum to dense shrubs, the 8–14-μm band-averaged emissivity increases from 0.940–0.986. We applied the volumetric model with the exponent bF ranging from 0.1, which corresponds to 10% coverage, to 2.9, which corresponds to nearly full coverage. The facet reflectance ρ was set to that of green leaves from the Salisbury measurements [4], and the facet transmission was set to zero. The soil reflectance ρ_0 was set to Salisbury's soil number 3721, which was an aridisol from Syria. We ran the model and integrated the results over the 8–14 μm range used in the Van de Griend study. The resulting emissivities ranged from 0.945 to 0.987. This represents a close agreement with measurements. The low LAI value is dependent, however, on the soil reflectance, which varies much more than green leaf reflectance. We obtained similar results for the high LAI value using a spectral reflection technique with a sample of leaves and soil $(\varepsilon \simeq 0.98)$ [7].

Olioso's theoretical study [33] determined that with leaf component emissivities ranging from 0.90 to 1.0, the canopy emissivity ranges from 0.96 to 1.0. This agrees with our volumetric predictions. This study also concluded that canopy emissivity with LAI $= 1.0$ was almost independent of zenith angle up to 60°, as is predicted by the volumetric kernels. This study and a follow-on study of the savanna data by Van de Griend [27] indicate that there is a significant empirical correlation between normalized difference vegetation index (NDVI) and the 8–14 μm emissivity. For a given scene, NDVI, LAI, and the exponent bF in the volumetric model are closely related. Therefore, the modified volumetric model not only substantiates the NDVI-emissivity correlation but also provides physical insight into the confounding factors, such as the soil reflectance.

For values of roughness $0.02 < \sigma < 0.20$, the BRDF of specular surfaces such as ice and water change significantly. The roughness spreads out the specular return. The directional-hemispherical properties, however, do not change very much. In a sense, as the roughness increases, the light from a given direction is scattered differently, but it goes somewhere in the hemisphere, so the integrated value is the same. Salisbury's measurements of smooth and rough distilled water ice [4] show a slight decrease in reflectance from 0.03 to 0.02, respectively ($\varepsilon = 0.97$ to $\varepsilon = 0.98$). Our single-scattering specular model predicts a decrease in directional-hemispherical reflectance near nadir of less than 0.001 when going from smooth to rough ice. The measured decrease is 0.01, probably because of shadowing and multiple scattering not accounted for by the model. The model reflectance for ice (and water) decreases more significantly with roughness at large angles. Our results are consistent with a theoretical analysis of water emissivity

versus wind speed and angle, using the original form of the Cox and Munk model, by Masuda *et al.* [34].

IV. Conclusions

We investigated the applicibility of reciprocity to BRDF models that relate component properties to structured scene properties. Models and proofs suggest that reciprocity generally holds for conventional structured surfaces, and there are no conclusive violations in measurements. Reciprocity guarantees that $\varepsilon(\theta) = 1 - \rho(\theta)$; so it is important when a model is to be used for reflectance and emissivity. Several reciprocal linear models were modified and applied to predict thermal infrared scene properties from measured component spectra.

The examples illustrate some important angular emissivity effects that the models reveal. With foliage as modeled by the volumetric kernels, there is little angular dependence of the scene emissivity. The shape of the dense canopy BRDF is fairly isotropic with some variation at large angles that depends on the ratio of leaf reflectance and transmission. Because of reciprocity, the more isotropic the BRDF, the smaller the angular dependence of the directional-hemispherical reflectance and emissivity. On the other hand, the geometrical examples demonstrate that there can be surprisingly large angular dependence of the scene emissivity even with Lambertian components. This is because of structure—primarily because of the changing viewed proportions of the components. Another effect of going from components to the scene is that the spectral contrast is reduced. Components will rarely have spectral features in the same place, so a mixture of components will have an averaging effect on the resulting spectrum.

The principles used for modeling in the reflective spectral range appear to apply in a straightforward manner to the thermal infrared. When the models are expressed in terms of BRDF, they can be integrated to give reflectance and emissivity of structured scenes. In particular, linear kernel models of BRDF may be preintegrated and applied to convert component spectra to scene properties in an efficient manner. The models are sufficient for qualitative explorations of angular effects and for studies of the relative variations. Existing measurements lend credence to the models, but further work is needed to validate absolute emissivity estimates, which should include comparisons with simulations, tower measurements, and the emissivity recovered by other methods, such as multichannel aircraft and satellite data.

Acknowledgment

The authors wish to thank J. Salisbury at the Johns Hopkins Applied Physics Laboratory for spectral data and W. Wanner of Boston University for suggesting the linear kernel approach for our BRDF studies.

References

[1] F. Nicodemus, J. Richmond, J. Hsia, I. Ginsberg, and T. Limperis, *Geometrical Considerations and Nomenclature for Reflectance*. Washington, DC: Hemisphere, 1977.

[2] C. D. Elvidge, "Thermal infrared reflectance of dry plant materials: 2.5–20.0 μm, *Remote Sens. Environ.*, vol. 26, pp. 265–285, 1988.

[3] J. W. Salisbury, L. S. Walter, N. Vergo, and D. M. D'Aria. *Infrared* (2.1–25 μm) *Spectra of Minerals*. Baltimore, MD: Johns Hopkins Univ. Press, 1991.

[4] J. W. Salisbury and D. M. D'Aria, "Emissivity of terrestrial materials in the 8–14 μm atmospheric window," *Remote Sens. Environ.*, vol. 42, pp. 83–106, 1992.

[5] ——, "Emissivity of terrestrial materials in the 3–5 μm atmospheric window," *Remote Sens. Environ.*, vol. 47, pp. 345–361, 1994.

[6] J. W. Salisbury, D. M. D'Aria, and A. Wald, "Measurements of thermal infrared spectral reflectance of frost, snow, and ice," *J. Geophys. Res.*, vol. 99, pp. 24 235–24 240, 1994.

[7] W. C. Snyder, Z. Wan, Y. Zhang, and Y. Feng, "Thermal infrared (3–14 μm) bidirectional reflectance measurements of sands and soils," *Remote Sens. Environ.*, vol. 60, pp. 101–109, 1997.

[8] T. Nilson and A. Kuusk, "A reflectance model for the homogeneous plant canopy and its inversion," *Remote Sens. Environ.*, vol. 27, pp. 157–167, 1989.

[9] J. Roujean, M. Leroy, and P. Deschamps, "A bidirectional reflectance model of the earth's surface for correction of remote sensing data," *J. Geophys. Res.*, vol. 97, pp. 20 455–20 468, 1992.

[10] W. Wanner, X. Li, and A. Strahler, "On the derivation of kernels for kernel-driven models of bidirectional reflectance," *J. Geophys. Res.*, vol. 100, pp. 21 077–21 089, 1995.

[11] A. H. Strahler, A. Moody, E. F. Lambin, A. Huete, C. Justice, J.-P. Muller, S. Running, V. Salomonson, V. Vanderbilt, and Z. Wan, "MODIS BRDF/albedo product: Algorithm Technical Basis Doc., Ver. 3.1, NASA EOS-MODIS," 1995.

[12] P. Lewis, "The utility of kernel-driven BRDF models in global BRDF and albedo studies," in *Proc. IGARSS'95*, vol. 2, pp. 1186–1188.

[13] Z. Wan and J. Dozier, "A generalized split-window algorithm for retrieving land-surface temperature from space," *IEEE Trans. Geosci. Remote Sensing*, vol. 34, pp. 892–905, 1996.

[14] R. Siegel and J. R. Howell, *Thermal Radiation Heat Transfer*, 2nd ed. Washington, DC: Hemisphere, 1981.

[15] F. Nicodemus, "Reflectance nomenclature and directional reflectance and emissivity," *Appl. Opt.*, vol. 9, pp. 1474–1475, 1970.

[16] F. Clarke and D. Parry, "Helmholtz reciprocity: Its validity and application to reflectometry," *Light. Res. Technol.*, vol. 17, pp. 1–11, 1985.

[17] F. Nicodemus, *Radiometry*, volume IV of *Applied Optics and Optical Engineering*, vol. 4. New York: Academic, 1967.

[18] J. Snell, *Radiometry and Photometry, Handbook of Optics*, vol. I. New York: McGraw-Hill, 1978.

[19] W. Rees, *Physical Principles of Remote Sensing*. Cambridge, U.K.: Cambridge Univ. Press, 1990.

[20] A. T. DeHoop, "Reciprocity theorem for the electromagnetic field scattered by an obstacle," *Appl. Sci. Res. B*, vol. 8, pp. 135–140, 1960.

[21] M.-J. Kim, "Verification of the reciprocity theorem," *Appl. Opt.*, vol. 27, pp. 2645–2646, 1988.

[22] W. C. Snyder, "BRDF reciprocity in measurements and modeling of structured surfaces," *IEEE Trans. Geosci. Remote Sensing*, to be published.

[23] X. Li and A. H. Strahler, "Geometric-optical bidirectional reflectance modeling of the discrete crown vegetation canopy: Effect of crown shape and mutual shadowing," *IEEE Trans. Geosci. Remote Sensing*, vol. 30, pp. 276–291, 1992.

[24] J. R. Irons, G. S. Campbell, J. M. Norman, D. W. Graham, and W. M. Kovalick, "Prediction and measurement of soil bidirectional reflectance," *IEEE Trans. Geosci. Remote Sensing*, vol. 32, pp. 249–259, 1992.

[25] A. H. Strahler and D. L. B. Jupp, "Modeling bidirectional reflectance of forests and woodlands using boolean models and geometric optics," *Remote Sens. Environ.*, vol. 34, pp. 153–166, 1990.

[26] J. K. Ross, *The Radiation Regime and Architecture of Plant Stands*. The Hague, The Netherlands: W. Junk, 1981.

[27] A. A. Van de Griend and M. Owe, "On the relationship between thermal emissivity and the normalized difference vegetation index for natural surfaces," *Int. J. Remote Sensing*, vol. 14, pp. 1119–1131, 1993.

[28] C. Cox and W. Munk, "Measurement of the roughness of the sea surface from photographs of the Sun's glitter," *J. Opt. Soc. Amer.*, vol. 44, pp. 838–850, 1954.

[29] S. P. Ahmad and D. W. Deering, "A simple analytical function for bidirectional reflectance," *J. Geophys. Res.*, vol. 97, pp. 18 867–18 886, 1992.

[30] W. Wanner, X. Li, and A. H. Strahler, "A new class of geometric-optical semiempirical kernels for global BRDF and albedo modeling," in *Proc. IGARSS'95*, vol. 1, pp. 15–17.

[31] B. Hu, W. Wanner, X. Li, and A. H. Strahler, "Valuation of kernel-driven semiempirical BRDF models for application to MODIS/MISR

data," in *Proc. IGARSS'96*, vol. 3, pp. 1669–1671.
[32] A. A. Van de Griend, M. Owe, M. Groen, and M. P. Stoll, "Measurement and spatial variation of thermal infrared surface emissivity in a savanna environment," *Water Resources Res.*, vol. 27, pp. 371–379, 1991.
[33] A. Olioso, "Simulating the relationship between thermal emissivity and the normalized difference vegetation index," *Int. J. Remote Sensing*, vol. 16, pp. 3211–3216, 1995.
[34] K. Masuda, T. Takashima, and Y. Takayama, "Emissivity of pure and sea waters for the model sea surface in the infrared window regions," *Remote Sens. Environ.*, vol. 24, pp. 313–329, 1988.

William C. Snyder (S'93–M'95) received the B.S. degree in engineering and applied science from the California Institute of Technology, Pasadena, in 1982 and the Ph.D. degree in imaging science from the Rochester Institute of Technology, Rochester, NY, in 1994.

After completing the Ph.D. degree, he studied the spectral infrared properties of natural surfaces as an Associate Member of the NASA MODIS Science Team, Institute for Computational Earth System Science, University of California, Santa Barbara. He is now continuing to work on optical modeling of surfaces, pattern recognition, and quantitative image processing at GDE Systems, Inc., San Diego, CA.

Zhengming Wan (S'81–M'84) received the B.A. degree from the University of Science and Technology of China in 1965 and the Ph.D. degree from the University of California, Santa Barbara (UCSB), in 1985.

He is with the Institute for Computational Earth System Science, UCSB. He is a member of the MODIS Science Team and a principal investigator in NASA's Earth Observing System (EOS). His main research activities are in radiative transfer simulation and modeling of the Earth system and applications of remote sensing techniques.